International Journal of Plasticity 104 (2018) 134–146

Contents lists available at ScienceDirect

International Journal of Plasticity

journal homepage: www.elsevier.com/locate/ijplas

Disconnections, dislocations and generalized disclinations in grain boundary ledges

X.Y. Sun[a], C. Fressengeas[b], V. Taupin[b], P. Cordier[a,*], N. Combe[c]

[a] Unité Matériaux et Transformations, Université Lille/CNRS, 59655 Villeneuve d'Ascq, France
[b] Laboratoire d'Etude des Microstructures et de Mécanique des Matériaux, Université de Lorraine/CNRS, 7 rue Félix Savart, 57073 Metz Cedex 3, France
[c] Centre d'Elaboration de Matériaux et d'Etudes Structurales, CNRS/Université de Toulouse, 29 rue J. Marvig, BP 94347, 31055 Toulouse Cedex 4, France

A B S T R A C T

The structure of ledges in otherwise symmetrical tilt boundaries built from atomistic simulations is investigated in copper in terms of continuous dislocation and generalized disclination fields. A "discrete-to-continuum" crossover method is used to build the relevant kinematic and defect density fields on the basis of discrete atomic displacements appropriately defined in the boundary area. The resulting structure of incompatibility is compared with the so-called disconnection model of boundary ledges. In addition to their dislocation content, which characterizes the elastic displacement discontinuity across the boundary, the ledges appear to be characterized by discontinuities of the elastic rotation and dilatation fields, which are reflected by non-vanishing generalized disclination density fields.

1. Introduction

Perfectly straight symmetrical tilt boundaries have been used as textbook examples to build models aimed at investigating the structure and energy distribution of grain boundaries at interatomic resolution length scale, as well as their migration under stress. Early models of planar grain boundaries were based on surface-dislocation densities, which were seen as the source of disorientation between grains (Frank, 1950; Bilby, 1955). In this interpretation, any arbitrary disorientation can be accommodated by an appropriate distribution of surface-dislocations. These models are efficient at predicting geometrical properties of planar grain boundary migration, such as the coupling factor relating the normal tilt boundary displacement to an imposed shear displacement (Cahn et al., 2006). However, surface-dislocations-based models are necessarily limited to small misorientation angles. Indeed, as implied by Frank's equation the density of surface-dislocations increases with the misorientation angle to the point where dislocation core overlapping occurs at high angles (Li, 1972). In addition, surface-dislocations are singularly supported by an infinitely thin interface, a premise at odds with high resolution observation of the atomistic structure of grain boundaries, which reveals periodic arrays of elementary units spreading over a finite-width layer, perhaps as thin as a nanometer, but definitely not vanishingly thin. Atomistic modeling has yielded a detailed understanding of the distribution of elastic energy in terms of these structural units (Sutton and Vitek, 1983; Spearot et al., 2007; Wang et al., 2014) and have provided mechanisms for boundary migration under stress (Cahn et al., 2006; Farkas et al., 2006; Tucker et al., 2010; Prieto-Depedro et al., 2015), at the price of heavy computational costs however. In parallel with these developments, continuous representations of grain boundaries have also been found useful, because they allow

* Corresponding author.
E-mail address: patrick.cordier@univ-lille1.fr (P. Cordier).

https://doi.org/10.1016/j.ijplas.2018.02.003
Received 25 October 2017; Received in revised form 5 February 2018; Accepted 6 February 2018
Available online 10 February 2018
0749-6419/ © 2018 The Authors. Published by Elsevier Ltd. This is an open access article under the CC BY-NC-ND license (http://creativecommons.org/licenses/BY-NC-ND/4.0/).

analyzing dissipative and diffusive phenomena at time-scales beyond the limits inherent to atomistic simulations, and because they lend themselves more easily to coarse-graining procedures. Such approaches include representations of grain boundaries at interatomic resolution length scale in terms of arrays of disclination dipoles regularly spaced along the boundary (Li, 1972; Shi and Li, 1975; Gertsman et al., 1989; Fressengeas et al., 2014), or analyzes at a larger scale (Warner et al., 2006; Berbenni et al., 2013; Upadhyay et al., 2016). In addition to retrieving the core energy of the tilt boundaries at all misorientations (Fressengeas et al., 2014), the disclination dipole model allows capturing the correct dependence of shear coupled boundary migration on the misorientation angle (Taupin et al., 2013, 2014). These results suggest that a continuous description involving displacement and crystal defect density fields that are smooth over a length scale of interatomic spacing can be adequate for the purpose of describing boundaries at this scale, and may usefully complement atomistic representations.

However, observations show that grain boundaries involve various defects affecting their periodic arrangements, such as atomic inclusions, kinks, ledges and local curvatures, whose role is often overlooked (McDowell, 2010). Indeed, the motion of a planar grain boundary under stress is unlikely to happen uniformly over large areas. Rather, small patches bounded by ledge loops should spread sidewise through tangential motion of the latter along the boundaries. Such a mechanism is known to control the kinetics of precipitation or dynamic recrystallization (Aaronson, 1962). It was recently observed in grain boundary migration under shear stress in ultra-fine-grained materials (Rajabzadeh et al., 2013). The involved interfacial line defects, here referred to as "ledges", have been modeled as "disconnections", which are characterized by a combined dislocation and step character (Hirth, 1994; Hirth and Pond, 1996). A crystallographic analysis allows to identify the potential Burgers vectors and step heights for a disconnection from the displacement shift complete (DSC) lattice of the bicrystal. However, due to its purely geometric nature, the ability of such an analysis to capture the dynamic properties of ledges is limited (Cahn et al., 2006). Being indicative of rotation and strain discontinuities across bounded surfaces, generalized disclinations are also able to correctly describe the step character of ledges but, in contrast to disconnection steps, they additionally feature a dissipative dynamics through driving forces and mobility laws in the framework of a complete mechanical theory (Acharya and Fressengeas, 2012, 2015). Therefore we are interested in describing the elastic structure of an otherwise symmetrical tilt boundary containing ledges in terms of smooth dislocation and generalized disclination density fields, together with the relevant kinematic fields: the elastic displacement vector and first- and second-order distortion tensor fields. Note that using standard disclinations in this model instead of generalized disclinations would have restricted the analysis to steps involving only a rotation discontinuity. This continuous rendering of the defected boundary is built on its discrete atomistic representation, as obtained from molecular dynamic simulations, by using the "discrete-to-continuum" crossover method introduced in (Sun et al., 2016a).

The paper is organized as follows. In Section 2, the atomic modeling of a $\Sigma 17(410)$ tilt boundary in a copper bicrystal involving ledges and the techniques bridging the discrete atomistic and continuum representations are briefly recalled, together with a primer on the continuous representation of crystal defects in terms of dislocation and generalized disclination fields. Section 3 provides a description of the ledges in terms of dislocation and generalized disclination fields, and compares with the structure of a straight symmetrical tilt boundary. A discussion of these results is provided in Section 4, through comparisons between the structure of incompatibility revealed by this analysis along the boundary and the disconnection model of ledges. The following conclusions focus in particular on the potential applications of the present results to the study of the dynamics of ledges and migrating boundaries. The mathematical notations are provided in the Appendix.

2. Atomistic modeling and continuous representation of ledged tilt boundaries

2.1. Atomistic description

We briefly present the molecular dynamic simulations used to generate the present boundary configurations. A detailed account can be found in (Combe et al., 2016). In shear-coupled boundary migration, the relative in-plane displacement u_t of two grains across their planar boundary is accompanied by a displacement u_n of the boundary normal to its plane. The coupling factor $\beta = u_n/u_t$ characterizes the boundary migration. Depending on the temperature and shearing velocity (Cahn et al., 2006; Combe et al., 2016; MacKain et al., 2017) or the normal stress (Combe et al., 2017)), different migration mechanisms corresponding to different coupling factors can be activated. Here, we chose to analyze the $\Sigma 17(410)[001]$ tilt boundary in copper, for which two mechanisms have been evidenced: the $\langle 100\rangle$ mode characterized by a coupling factor $\beta = 1/2 > 0$ and the $\langle 110\rangle$ mode with a coupling factor $\beta = -6/5 < 0$ (Cahn et al., 2006), because this duality confers a wider perspective to our work. The simulations were conducted using the molecular dynamics package LAMMPS (Plimpton, 1995) with the embedded atom potential provided in (Mishin et al., 1999). The simulation cell contained 15 680 atoms in two symmetrical perfect copper crystals misoriented by a 28.07° angle about the [001] direction. Its dimensions were respectively $11.8nm$, $10.7nm$ and $1.4nm$ along the orthonormal basis $(\mathbf{e}_1, \mathbf{e}_2, \mathbf{e}_3)$ laid in the upper crystal directions ($[\bar{1}40]$, [410], [001]) (see Fig. 1). In addition, two slabs $1.6nm$-thick at the top and bottom of the simulation cell in the $\mathbf{e}_2$ direction were frozen in the perfect lattice configuration. Periodic boundary conditions were applied in the $\mathbf{e}_1$ and $\mathbf{e}_3$ directions. The relative displacement u_t of the perfect slabs in the $\mathbf{e}_1$ direction produces a shear stress σ_{12} on the bicrystal, which induces boundary migration. The Nudge Elastic Band (NEB) method is applied to determine the minimum energy path between the initial and final configurations defined below. The migration is produced by shearing the equilibrium configuration in Fig. 1 a. used as the initial configuration, respectively at $400K$ with the shearing velocity $9.4 \times 10^{-3} m.\, s^{-1}$ under the $\langle 100\rangle$ mode and at $0K$ under the $\langle 110\rangle$ mode. Note that this shearing velocity is of the order of velocities used in (Cahn et al., 2006). The atomic configurations after migration (quenched to $0K$ for the $\langle 100\rangle$ mode) are elastically unloaded at $0K$ to bring the slabs back to their initial positions. The resulting atomic configurations are the final configurations of the minimum energy paths and are shown in Fig. 1 b.c. The calculations involved respectively 80 and

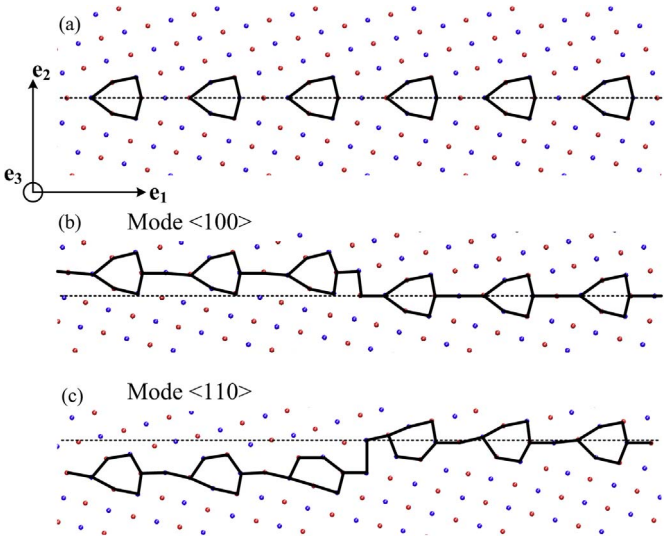

Fig. 1. Initial equilibrium configuration of the straight symmetrical Σ17(410) tilt boundary in a copper bicrystal misoriented by a 28.07° angle about the [001] direction (a). Final configurations along the minimum energy path showing ledges moving to the right in the ⟨100⟩ upward migration mode at 400K (b) and the ⟨110⟩ downward mode at 0K (c). Horizontal dotted lines sketch the initial position of the grain boundary. Red/blue balls represent atoms belonging to two consecutive planes normal to $\mathbf{e}_3$. The period of the simulation cell is about three times longer than the figure in direction $\mathbf{e}_1$. (For interpretation of the references to colour in this figure legend, the reader is referred to the Web version of this article.)

800 NEB images in the ⟨110⟩ and ⟨100⟩ modes. They show that the boundary migration occurs through the nucleation and sidewise motion in opposite directions of two ledges (Rajabzadeh et al., 2014; Combe et al., 2016). Fig. 1 b.c features the ledges moving to the right when a positive shear stress is applied. Arrays of kite-shaped structural units pointing to the left are also revealed along the boundary in both modes. In mode ⟨100⟩, the structural units exhibit symmetry with respect to the interface and seem only slightly distorted when passed by the ledge, whose height is of the order of 2 Å (see Fig. 1b). In mode ⟨110⟩ (see Fig. 1c), the step height is about 2.5 Å and the structural units are seen to be significantly distorted in the ledge's wake. Analyzing the involved displacements and distortions with the tools of continuum mechanics is instrumental in the following. Only the ledges shown in Fig. 1 were analyzed, and we expect that our results can be extended by symmetry to the ledges not shown here.

2.2. From atomistic to continuum description of grain boundaries

The atomic locations in reference and current configurations are used to build the continuous representation of the grain boundary. In the present case, the reference configuration is chosen to be the relaxed configuration of the boundary after shear, as determined in Section 2.1, and the current configuration is the perfect lattice based on the atomic positions on a relaxed boundary with a ledge. At first, the discrete values of the elastic displacement field $\mathbf{u}_e = \mathbf{x} - \mathbf{X}$ are calculated at each atom location in the boundary area. Here, the vectors $\mathbf{X}$ and $\mathbf{x}$ reflect the atomic positions in the reference and current state, respectively. Then the components $U^e_{ij} = u^e_{i,j}$ and $G^e_{ijk} = u^e_{i,jk}$ in the orthonormal frame ($\mathbf{e}_1$, $\mathbf{e}_2$, $\mathbf{e}_3$) of the elastic first-and second-order distortion fields ($\mathbf{U}_e$, $\mathbf{G}_e$) are calculated through finite difference schemes. Further, the dislocation and generalized-disclination density fields ($\boldsymbol{\alpha}$, $\boldsymbol{\pi}$) are found from the relations (1,7,11) discussed below. Because they encounter discontinuities across bounded surfaces as will be seen in Section 2.3, we use a backward Euler finite difference scheme to differentiate the displacement and first-order distortion fields, and a forward Euler finite difference scheme for the second-order distortion field because it has sufficient continuity across these surfaces. Finally, all atoms are projected onto the plane ($\mathbf{e}_1$, $\mathbf{e}_2$) in Fig. 1, and two-dimensional interpolation in this plane is used to take advantage of the symmetries of the crystal. The contour lines of all fields are plotted by using the following steps. All atoms are connected to tile the ($\mathbf{e}_1$, $\mathbf{e}_2$) plane with non-overlapping Delaunay triangles. The intersections of the contour lines with the triangles edges are determined by linear interpolation, and are eventually connected by bi-harmonic spline functions to generate smooth lines. Higher-order interpolation schemes are possible by selecting more than two neighboring atoms for a given target-point, but they do not improve significantly the results because the triangle edges are most often the steepest-descent lines for the jumps occurring between two atoms. The fundamentals of this discrete-to-continuum crossover method were presented with more details in (Sun et al., 2016a) where it was applied to a Σ37(610)[100], 18.9° symmetrical tilt boundary in copper as a benchmark test, and its accuracy validated by comparison with similar techniques recently published (Gullett et al., 2008; Zimmerman et al., 2009; Tucker et al., 2011). Additional details were provided in (Sun et al., 2017) in the course of studying tilt boundaries in MgO.

2.3. Discontinuity and incompatibility in defected crystals

In his seminal 1907 paper, Volterra introduced six types of crystal line defects (Volterra, 1907). Three of them, known as

dislocations, are translational defects. The other three, referred to as disclinations, have rotational character. In the sole presence of dislocations, the elastic displacement field $\mathbf{u}_e$ of the dislocations features a discontinuity $[\![\mathbf{u}_e]\!]$ across (non-unique) smooth surfaces bounded by the dislocation lines, but the elastic distortion (strain and rotation) field $\mathbf{U}_e$ displays continuity in non-simply-connected domains excluding their lines. A line integral of the elastic distortion field along any curve encircling the dislocation line, *i.e.* a Burgers circuit, yields the constant vector $\mathbf{b} = [\![\mathbf{u}_e]\!]$ equal to the discontinuity of the elastic displacement and referred to as the Burgers vector of the dislocation. Instead of Volterra's discrete representation of dislocations, we use here a continuous setting where this description is regularized by acknowledging the existence of a finite dislocation core region. In this description, the elastic displacement field is continuous across the dislocation core, but a Burgers circuit sufficiently distant from the core still leads to the non-zero Burgers vector **b**. We consider smooth elastic distortion fields in simply connected domains including the core, which are irrotational outside the core, but whose non-vanishing curl defines a smooth dislocation density tensor field inside the core:

$$\boldsymbol{\alpha} = \mathbf{curl}\ \mathbf{U}_e. \tag{1}$$

In the absence of disclinations, the Burgers vector can be computed from a surface integral of the tensorial density $\boldsymbol{\alpha}$ over appropriate patches S (see below Eq. (6)). In the additional presence of disclinations, a discontinuity $[\![\omega_e]\!]$ in the elastic rotation tensor fields ω_e occurs over a surface terminating at the disclination line. Hence, smoothness of the elastic distortion field is lost, but the elastic strain field ε_e retains continuity across this surface, except at the dislocation line where it has a singularity. The disclinations are characterized by their Frank vector $\boldsymbol{\Omega} = [\![\vec{\omega}_e]\!]$, which represents the magnitude and direction of the discontinuity of the rotation vector over closed circuits encircling the disclination line. In deWit's continuous setting (deWit, 1970), also adopted in the present paper by acknowledging the finiteness of the core region of the disclinations, the smooth elastic curvature field is irrotational outside the disclination core, and the disclination density tensor is defined as the curl of this field inside the core:

$$\boldsymbol{\theta} = \mathbf{curl}\ \boldsymbol{\kappa}_e. \tag{2}$$

The tensors $\boldsymbol{\alpha}$ and $\boldsymbol{\theta}$ are smooth renditions of the Burgers and Frank vectors respectively. Indeed, the latter are obtained by performing the following integrations over a closed circuit C surrounding the surface patch S of unit normal **n**:

$$\boldsymbol{\Omega} = \int_C \boldsymbol{\kappa}_e.\ \mathbf{dr} \tag{3}$$

$$\mathbf{b} = \int_C (\boldsymbol{\varepsilon}_e - (\boldsymbol{\kappa}_e^t \times \mathbf{r})^t).\ \mathbf{dr}, \tag{4}$$

where the superscript t denotes a transpose (see notations in Appendix), but also on integrating respectively over S the disclination density tensor field:

$$\boldsymbol{\Omega} = \int_S \boldsymbol{\theta}.\ \mathbf{n} dS, \tag{5}$$

and a combination of the dislocation density tensor with a vectorial product of the disclination density tensor and the position vector **r**:

$$\mathbf{b} = \int_S (\boldsymbol{\alpha} - (\boldsymbol{\theta}^t \times \mathbf{r})^t).\ \mathbf{n} dS. \tag{6}$$

Eqs.(5) and (6) provide a direct link between the discontinuities of the elastic rotation and displacement and the smooth disclination and dislocation density fields. By choosing appropriately the integration patch S, it is possible to obtain the Frank and Burgers vectors of differential parts of the defects, as we shall see below in Figs. 3 and 5, or those of the whole defect. (Acharya and Fressengeas, 2012, 2015) adopted a similar approach in introducing the generalized disclinations (”g-disclinations”). The g-disclination concept goes beyond the Volterra construct in the sense that the elastic distortion field may now display a discontinuity $[\![\mathbf{U}_e]\!]$ in both rotation and strain across surfaces terminating at g-disclination lines. The characteristic tensor $\boldsymbol{\Pi}$ of the g-disclination is defined as the jump in the elastic distortion tensor field across such surfaces: $\boldsymbol{\Pi} = [\![\mathbf{U}_e]\!]$. In a continuous setting, the elastic second-order distortion field $\mathbf{G}_e$ is irrotational outside the core region of the g-disclination where $\mathbf{G}_e = \mathbf{grad}\ \mathbf{U}_e$, whereas its curl is non-zero inside the core where it provides for the definition of the third order g-disclination density tensor field $\boldsymbol{\pi}$:

$$\boldsymbol{\pi} = \mathbf{curl}\ \mathbf{G}_e. \tag{7}$$

The integration of $\mathbf{G}_e$ over closed circuits C surrounding patches S yields the jump of the elastic distortion tensor field:

$$\boldsymbol{\Pi} = \int_C \mathbf{G}_e.\ \mathbf{dr}. \tag{8}$$

Equivalently the integration of $\boldsymbol{\pi}$ over the patch S leads to:

$$\boldsymbol{\Pi} = \int_S \boldsymbol{\pi}.\ \mathbf{n} dS. \tag{9}$$

Eq. (9) provides a direct link between the discontinuity of the elastic distortion and the smooth g-disclination density field. The g-disclination density tensor $\boldsymbol{\pi}$ complements the standard disclination density $\boldsymbol{\theta}$ by possibly adding a discontinuity of strain to the rotation discontinuity. The following relation links these tensors at small transformations:

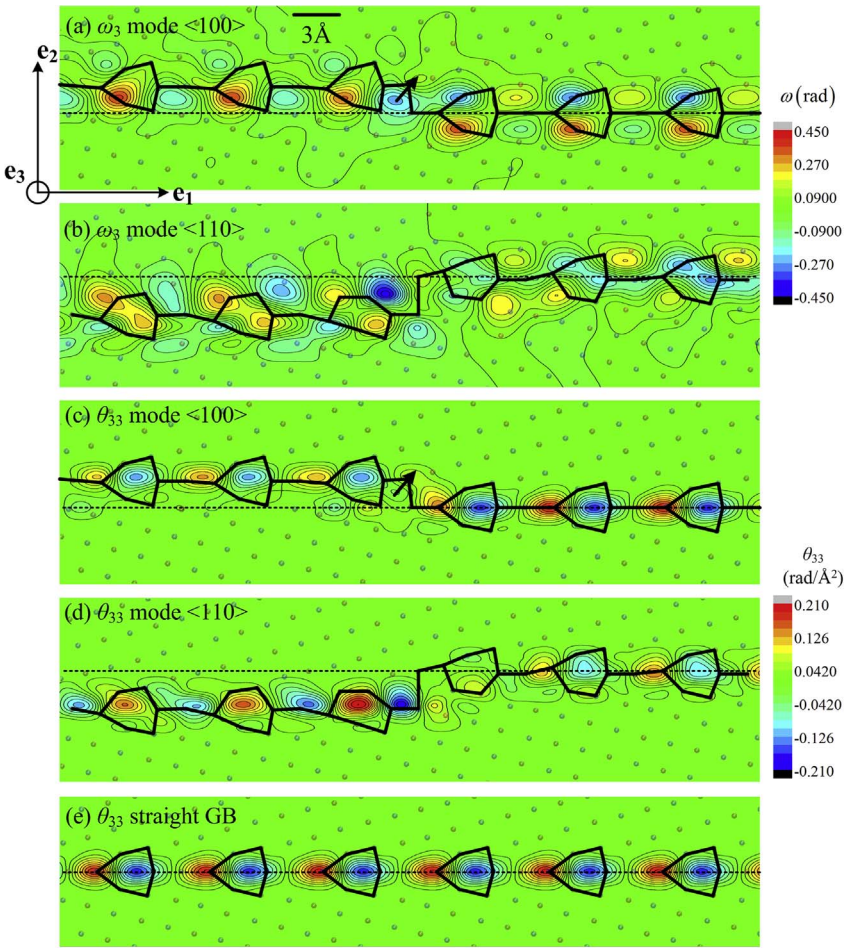

Fig. 2. Elastic rotation ω_3 and wedge disclination θ_{33} component fields on top of the lattice in tilt boundary Σ17(410) with <100> ledge (a,b) and <110> ledge (c,d). Wedge disclination θ_{33} field along the straight tilt boundary Σ17(410) (e). The black arrows in panels (a,c) underline the localized rotation patches in the ledge area, from negative to positive rotation, and the disclination dipole.

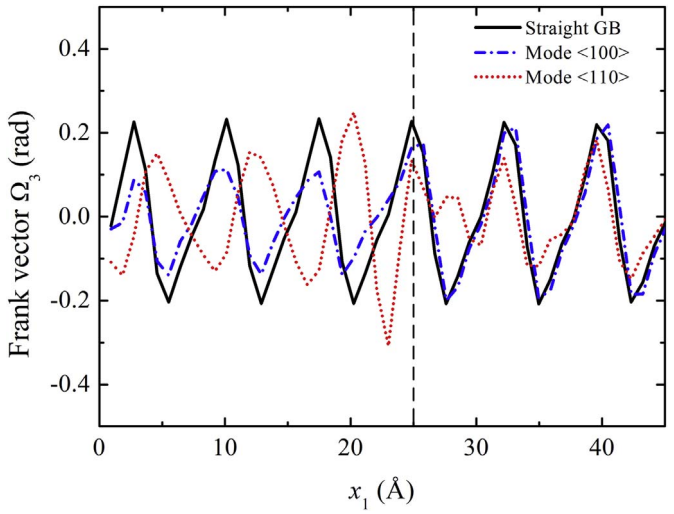

Fig. 3. Differential Frank vector component Ω_3 for straight tilt boundary Σ17(410) and tilt boundary Σ17(410) with <100> and <110> ledges. The ledge abscissa is 25 Å (vertical dashed line).

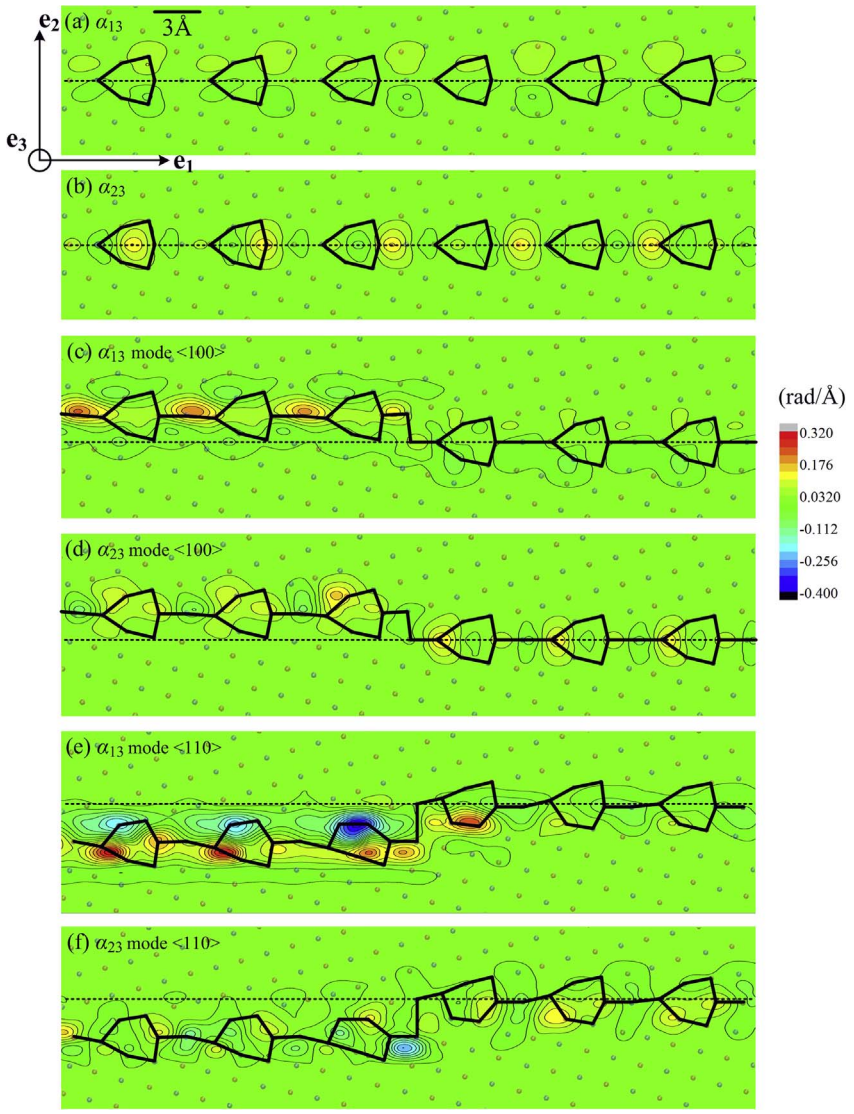

Fig. 4. Dislocation fields (α_{13}, α_{23}) on top of the lattice. Straight Σ17(410) tilt boundary (a,b), tilt boundary Σ17(410) with <100> ledge (c,d) and ⟨110⟩ ledge (e,f).

$$\boldsymbol{\pi} = \boldsymbol{\xi} - \mathbf{X}.\,\theta \tag{10}$$

where the third-order tensor $\boldsymbol{\xi}$ is associated with a discontinuity of the elastic strain tensor (and is therefore symmetrical in its first two indices) and $\mathbf{X}$ is the third-order (alternating) Levi-Civita tensor (see Appendix). When, as a special case, the elastic strain field retains continuity while the elastic rotation field presents a discontinuity, the g-disclinations reduce to standard disclinations. In the presence of g-disclinations, the dislocation density tensor $\boldsymbol{\alpha}$ cannot be defined through Eq. (1) as in the theory of dislocations, because $\mathbf{U}_e$ does not have anymore the continuity that is needed in this relation. Instead, $\boldsymbol{\alpha}$ is defined by alternating the 2-distortion tensor $\mathbf{G}_e$ as follows:

$$\boldsymbol{\alpha} = -\mathbf{G}_e : \mathbf{X}. \tag{11}$$

The Burgers vector is still obtained from Eq. (6) in the presence of g-disclinations, but with the dislocation density tensor given by Eq. (11). It is straightforward to show that Eq. (11) reduces to Eq. (1) when $\mathbf{G}_e = \mathbf{grad}\,\mathbf{U}_e$ in the absence of g-disclinations (see relation A-7 in the Appendix).

3. Continuous description of ledges

3.1. Standard disclinations

We start with the description of the ω_3 elastic rotation and θ_{33} wedge disclination density component fields shown in Fig. 2,

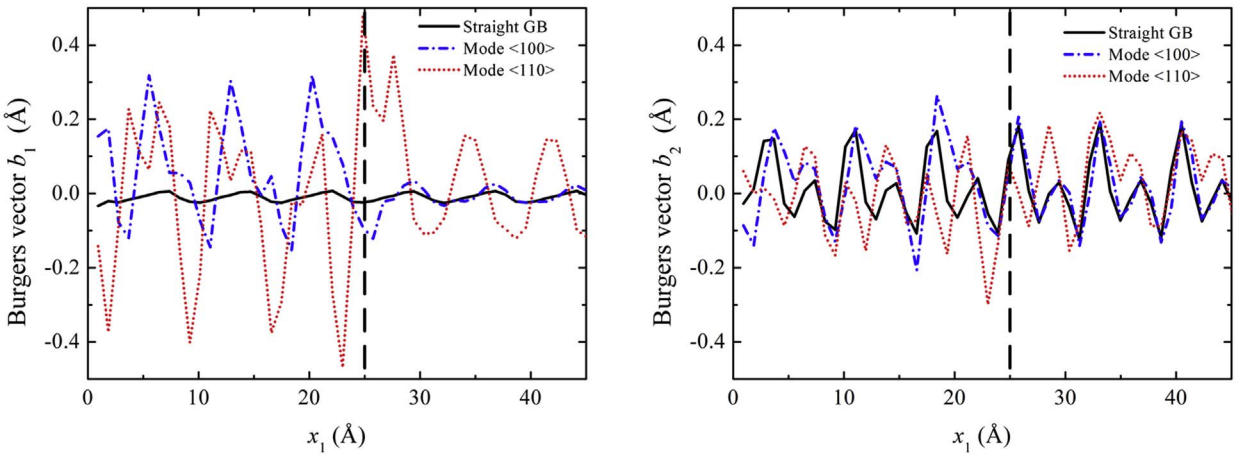

Fig. 5. Differential Burgers vector components (b_1, b_2) for the straight tilt boundary Σ17(410) and tilt boundary Σ17(410) with ⟨100⟩ and ⟨110⟩ ledges. The ledge abscissa is 25 Å (vertical dashed lines).

together with Ω_3 Frank's vector magnitude map in Fig. 3. The rotation field ω_3 is shown in panels (2.a,2.b) for the two ledge modes. It is essentially located within a nanometer thick layer along the boundary. For the upward ⟨100⟩ mode in panel (2.a), localized spots of strong opposite magnitudes are seen across the interface at the tip and basis of each structural unit, with a maximum local magnitude of the rotation of the order of 21° (0.38 rad). These spots are seen ahead of the advancing ledge (to the right of the ledge), but also to a lesser degree in its wake (to its left). The pair of rotation spots at the tip of the structural unit tends to ”open” the crystal and are associated with a positive wedge disclination, as shown in panel (2.c), whereas the rotation spots at the basis tend to “close” the crystal and are associated with a negative wedge disclination. The similarity of these rotation and disclination fields with their counterparts found in similar straight tilt boundaries (Fressengeas et al., 2014; Sun et al., 2016a) and in panel (2.e) is striking. The ledge area contains opening and closing rotation spots (marked with an arrow from closing to opening) at angle with the normal to the interface, but the disclination map in panel (2.c) is only slightly disturbed by the presence of the ledge. The “differential” Frank vector magnitude shown in Fig. 3 reflects closely this evolution. It is calculated by using rectangular integration slices 1 Å wide in the $\mathbf{e}_1$ direction and 10 Å high in the $\mathbf{e}_2$ direction as integration patches in Eq. (5). Note in particular that it decreases from head to tail of the ledge, which corresponds to a decreased overall curvature level. Its maximum value is of the order of 13° (0.225 rad). The rotation and disclination maps in the ⟨110⟩ downward mode follow similar evolutions in panels (2.b, 2.d), although the perturbations of the fields are much stronger in the ledge area than in the <100> mode. Again, this is closely reflected by the differential Frank vector size in Fig. 3, whose maximum value is 21°.

3.2. Dislocations

In a similar way, we now comment the edge dislocation fields (α_{13}, α_{23}) shown in Fig. 4 and, in Fig. 5, the ”differential” Burgers vector components (b_1, b_2) obtained by integrating over thin slices these two dislocation density fields and the wedge disclination density field θ_{33} according to Eq. (6). In panels (4.a,b), the α_{13} and α_{23} edge dislocation density fields for the straight tilt boundary Σ17(410) are found to be very similar to those previously obtained for a straight Σ37(610)[110], 18.9° tilt boundary in copper (Sun et al., 2016a). The Burgers vector is normal to the interface, as can be expected for a straight tilt boundary and as Fig. 5 shows. In panels (4.c,d), the distributions ahead of the ledge of α_{13} and α_{23} in mode <100> are similar to the fields in panels (4.a,b), but they strongly differ in the ledge's wake. This is indicative of very different incompatible distortion fields. In both modes, the α_{23} dislocation content and the normal component b_2 of the differential Burgers vector are of same order on both sides of the ledge, but strong α_{13} contents and longitudinal components b_1 of the Burgers vector are found in the ledge's wake, even more so in the <110> mode. In the ledge area, the dislocations are mostly α_{13} in both modes, with their differential Burgers vector in the longitudinal direction $\mathbf{e}_1$. Integrating the differential Burgers vectors over the whole ledge area using a slice 17.5 Å wide leads to the Burgers vector component of the ledge area $b_1 \cong 2.6$ Å in the <110> mode vs. $b_1 \cong 0.9$ Å in the <100> mode, in agreement with values provided in (Combe et al., 2016).

3.3. Generalized disclinations

It was observed in Σ9 silicon bicrystals (Couillard et al., 2013) and evidenced in smooth renditions of molecular dynamics simulations of tilt boundaries in copper using the present discrete-to-continuum technique (Sun et al., 2016a) that, besides the discontinuity in lattice rotation, straight symmetrical tilt boundaries may involve a discontinuity of the shear strain field. In the present interpretation, this discontinuity induces the presence of a non-vanishing smooth g-disclination field along the boundary. To illustrate this feature, the π_{123} and π_{213} fields corresponding to the shear strain discontinuity $[\![\varepsilon_{12}]\!]$ and rotation discontinuity $[\![\omega_3]\!]$ in the straight Σ17(410) tilt boundary in copper are shown in Fig. 6(c,e). Strikingly, dipoles similar to the standard disclination dipoles are

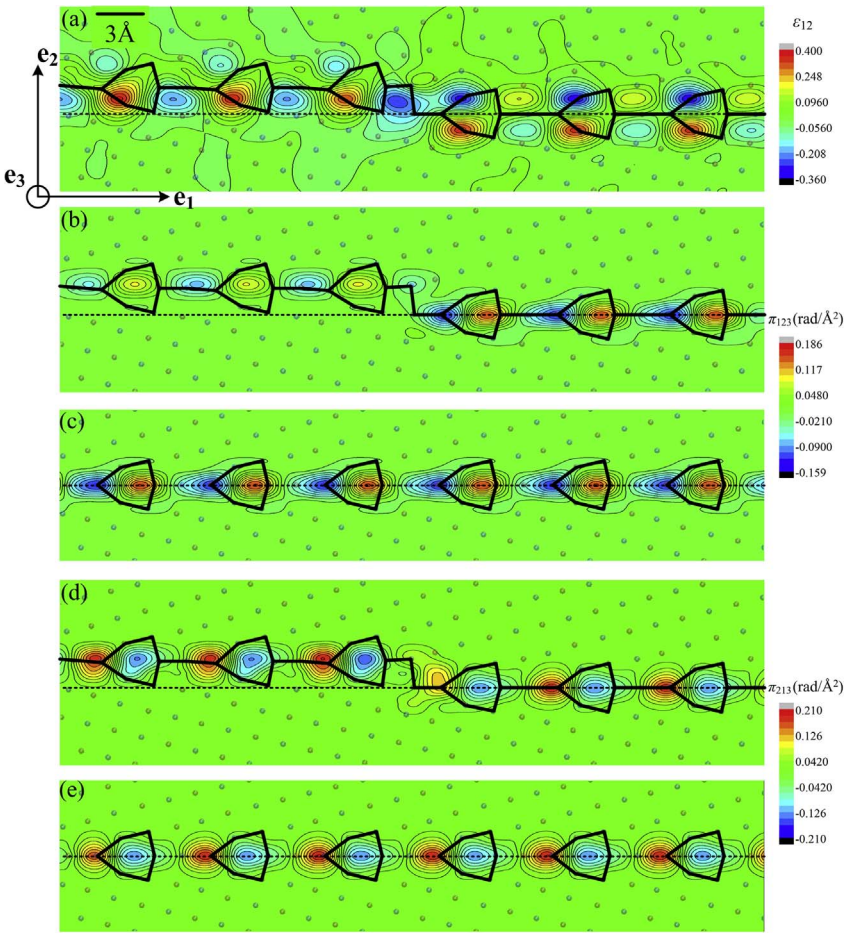

Fig. 6. Shear strain ε_{12} (a), g-disclination π_{123} (b) and π_{213} (d) fields on top of tilt boundary Σ17(410) with ⟨100⟩ ledge. G-disclination (c) π_{123} and (e) π_{213} fields of the straight Σ17(410) tilt boundary.

observed at the ends of the structural units, with inverse polarities for π_{123} and π_{213}. Since Eq. (10) reads here:

$$\pi_{123} = \xi_{123} - \theta_{33}$$

$$\pi_{213} = \xi_{213} + \theta_{33},$$

which entails $\xi_{123} = (\pi_{213} + \pi_{123})/2$ because $\xi_{123} = \xi_{213}$, the relative values of $(\pi_{123},\ \pi_{213})$ in Fig. 6(c,e) imply that the ξ_{213} dipoles have same polarity as the θ_{33} dipoles. Thus, besides the rotation discontinuity, the structural units support a shear strain discontinuity. In the presence of a ⟨100⟩ ledge along the boundary, the $(\pi_{123},\ \pi_{213})$ g-disclination fields displayed in panels (6.b,d), are very similar to their counterparts along the straight boundary shown in panels (6.c,e). Only limited perturbations are observed in the ledge area. To a lesser degree, similar observations can be made for the ⟨110⟩ mode, although less neatly and although the perturbations of the g-disclination fields in the ledge area are stronger (see Fig. 7).

More significant features are displayed by the stretch fields $U_{11} = \varepsilon_{11}$ and $U_{22} = \varepsilon_{22}$ along the boundary featuring a <100> ledge in Fig. 8 and a ⟨110⟩ ledge in Fig. 9. Strikingly, the $(U_{11},\ U_{22})$ fields are continuous across the interface, except in the ledge area where discontinuities[1] marked by arrows can be noticed. In mode ⟨100⟩ ledges, discontinuities $\Pi_{11} = [\![U_{11}]\!]$ and $\Pi_{22} = [\![U_{22}]\!]$ are seen in Fig. 8, but only a $\Pi_{22} = [\![U_{22}]\!]$ discontinuity can be noticed in the ⟨110⟩ mode in Fig. 9. Performing the integrations involved in Eq. (9) over a rectangular box including all of the g-disclination dipoles leads to the stretch discontinuities: $\Pi_{11} = 4.5\%$, $\Pi_{22} = 12\%$ in mode <100> ledges and $\Pi_{11} \cong 0$, $\Pi_{22} = 7.5\%$ in mode ⟨110⟩ ledges. Hence, these features, not seen with this intensity along straight tilt boundaries, appear to be characteristic of ledges. In terms of g-disclination densities, they are reflected by strong π_{113} and π_{223} dipoles in the ledge areas, as shown in Fig. 8(b,d) and Fig. 9c.

[1] In the present smooth representation of lattice incompatibility, strong variations of field variables within a very short distance are called discontinuities for their sharply defined distribution (Sun et al., 2016a, 2017). For example, the jump of U_{22} from 15% to − 20% in less than 3 Å in the ledge area in Fig. 8 c is called a discontinuity.

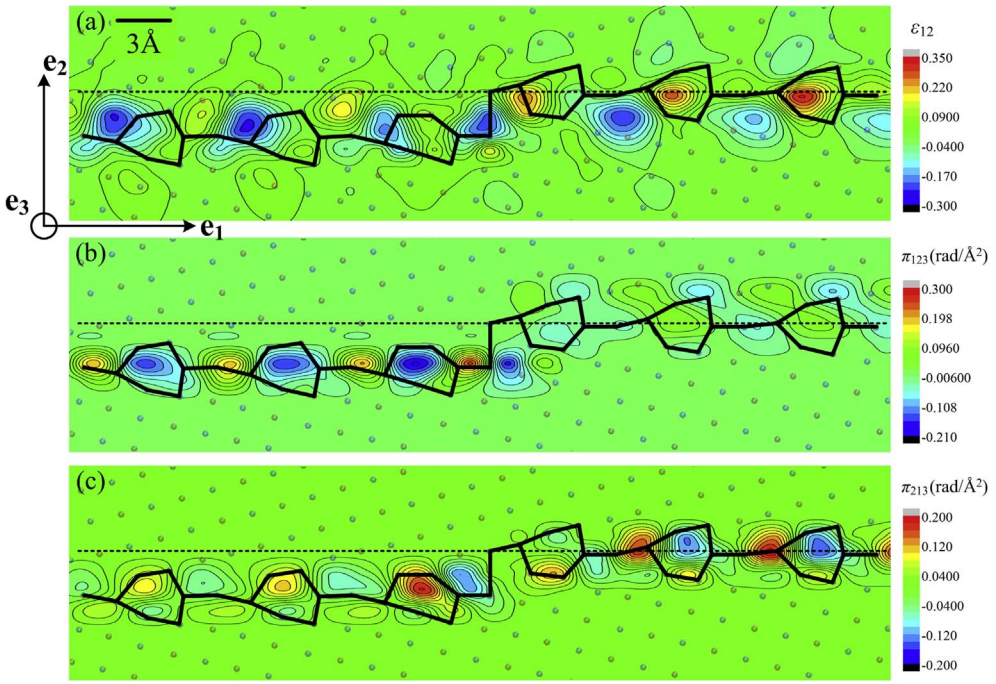

Fig. 7. In-plane shear strain ε_{12} (a), g-disclination π_{123} (b) and π_{213} (c) fields on top of tilt boundary Σ17(410) with ⟨110⟩ ledge.

4. Discussion

Following (Hirth, 1994; Hirth and Pond, 1996), the interfacial defects referred to above as ledges are described as *disconnections* exhibiting both dislocation and step character.[2] The Burgers vector of the dislocation component reflects the incompatibility of the elastic distortion needed to join the adjacent crystals when their corresponding surfaces are not complementary or when their relative positions break their complementarity. It can be determined by Burgers circuit mapping as in Eq. (4), or by integrating the dislocation/disclination densities over the appropriate surface as in Eq. (6), and as shown above. The step character of the disconnection is not seen as being the result of an incompatibility and is not determined by circuit mapping. Its height h is defined as the extent of material overlap normal to the interface when the adjacent crystals are placed together to make contact without imposing the elastic distortion needed to join their corresponding surfaces (Hirth and Pond, 1996). The representation of the ledges emerging from this model in the present Σ17(410) boundaries is displayed in Fig. 10. The step height h is simply the height of the ledge above the perfect interface in mode ⟨100⟩, or below this interface in mode <110> (see Fig. 10), and the Burgers vector of the dislocation component of the disconnection is longitudinal.

Clearly, the main difference between the disconnection model and the dislocation/g-disclination description of the ⟨100⟩ and ⟨110⟩ ledges through continuous rendering of their atomistic structure is that distortion incompatibility arises only from displacement discontinuity in the disconnection model, implying the sole presence of dislocations, whereas rotation and strain discontinuities are also involved in the present description of first- and second-order distortion incompatibility, which induces the additional presence of non-vanishing g-disclination fields. Concomitantly, the step character of the disconnection is absent *per se* from the description in terms of dislocations and g-disclinations. However, the information it contains also pertains to the description of second-order incompatibility, where it allows characterizing the rotation and strain closure defects. This is illustrated by the sketches in Fig. 11. In particular, the step height h can be viewed in this figure as the projection of the arm-length of the g-disclination dipole on the normal to the interface.

5. Summary and concluding remarks

The discrete-to-continuum crossover method of (Sun et al., 2016a) provides a continuous rendering of the atomistic structure of ⟨100⟩ and ⟨110⟩ ledges in a Σ17(410) tilt boundary in copper. The description of the imperfect boundary is given in terms of the displacement field with respect to the perfect lattice and the first-order distortion (rotation and strain) and second-order distortion fields. Discontinuities in displacement, rotation and strain are found across bounded areas along the boundary. In addition to

[2] The word *disconnection* has been used in (Fressengeas and Taupin, 2014, 2016) to define crystal defect densities in the presence of fracture, in reference to the disruption of material connectivity occurring in this context. Of course, such is not the case in the present analysis where continuity of the material is assumed throughout the paper.

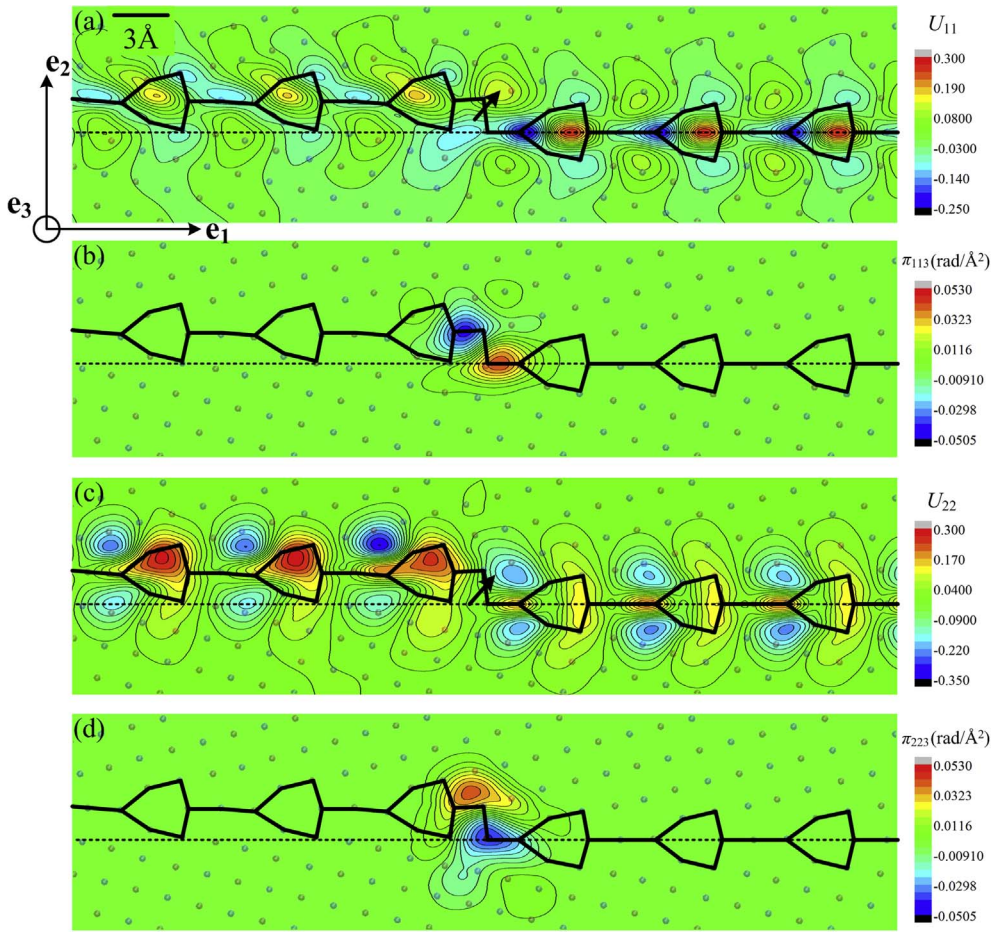

Fig. 8. In-plane distortion U_{11} (a), (b) g-disclination π_{113}, (c) U_{22}, and (d) g-disclination π_{223} fields on top of tilt boundary Σ17(410) with ⟨100⟩ ledge. The arrows underline the localized U_{11} and U_{22} spots in the ledge area.

discontinuities already found in the straight parts of the boundary and discussed earlier in several papers (Sun et al., 2016a, 2016b, 2017), significant displacement, rotation and stretch discontinuities are observed in the ledges areas. These discontinuities are reflected in the incompatibility of the first- and second-order distortions and in the dislocation and g-disclination density fields respectively. In particular, the occurrence of stretching g-disclination dipoles appears to be characteristic of the investigated ledges. This description is compared with the disconnection model of ledges, as proposed by (Hirth, 1994; Hirth and Pond, 1996) in terms of dislocations and steps.

The incompatibility of the first-order distortion and the dislocation fields are identical in the disconnection and dislocation/g-disclination models. Due to its geometrical nature, the step character of the disconnections is only indirectly linked with this incompatibility. In the present analysis, the step characteristics appear to be also associated with the incompatibility of the second-order distortion, as manifested by the presence of standard disclination and stretching g-disclination dipoles in the ledges areas. In contrast with the ”second-order” perception that may arise from this association, the step height is not a second-order effect, as its value may be comparable with or even larger than the magnitude of the Burgers vector of the defect. Such significant values derive from large rotation and stretch discontinuities in the ledge area.

Being interpreted in terms of g-disclination fields, the step fully participates to lattice incompatibility in the ledge area. Hence, ledges have an elastic energy not only from the incompatible strains associated with dislocations, but also from the incompatible second-order distortions associated with the g-disclinations, which includes the incompatible curvatures associated with standard disclinations. Their elastic properties and interactions with other crystal defects may therefore be interpreted by using the elastostatic equations of the mechanical theory of dislocation and g-disclination fields (Acharya and Fressengeas, 2012, 2015). Their evolutions in time may also be modeled by additionally employing the dynamic equations for plasticity and phase transformation introduced in this theory. In the latter, the dislocation and g-disclination fields have a natural dynamics through transport laws. Similar to dislocation densities, g-disclination densities are assigned velocities and Peach-Koehler-type driving forces. By relating velocities to driving forces, mobility laws compatible with the thermodynamic requirement for positive dissipation complete the description. When adequate mobility laws are chosen on physical grounds, the spatio-temporal evolutions of the displacement, dislocation and g-disclination fields can be deduced from the set of partial differential equations of the theory as the solution of

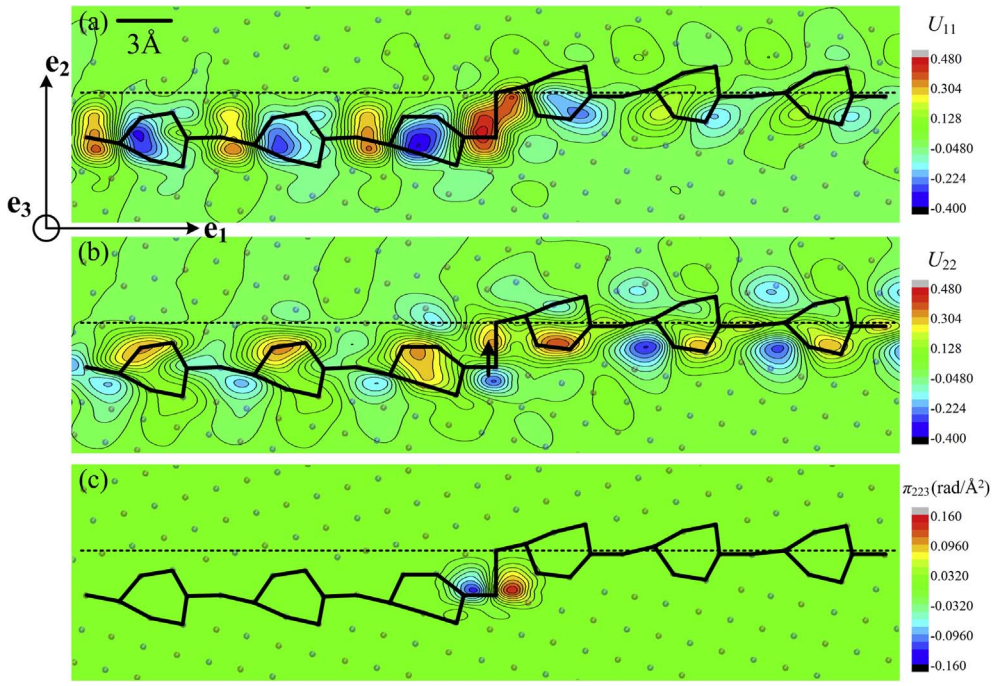

Fig. 9. In-plane distortion U_{11} (a), g-disclination π_{113} (b), in plane distortion U_{22} (c), and g-disclination π_{223} (d) fields on top of tilt boundary Σ17(410) with <110> ledge. The arrow underlines the localized U_{22} spot in the ledge area.

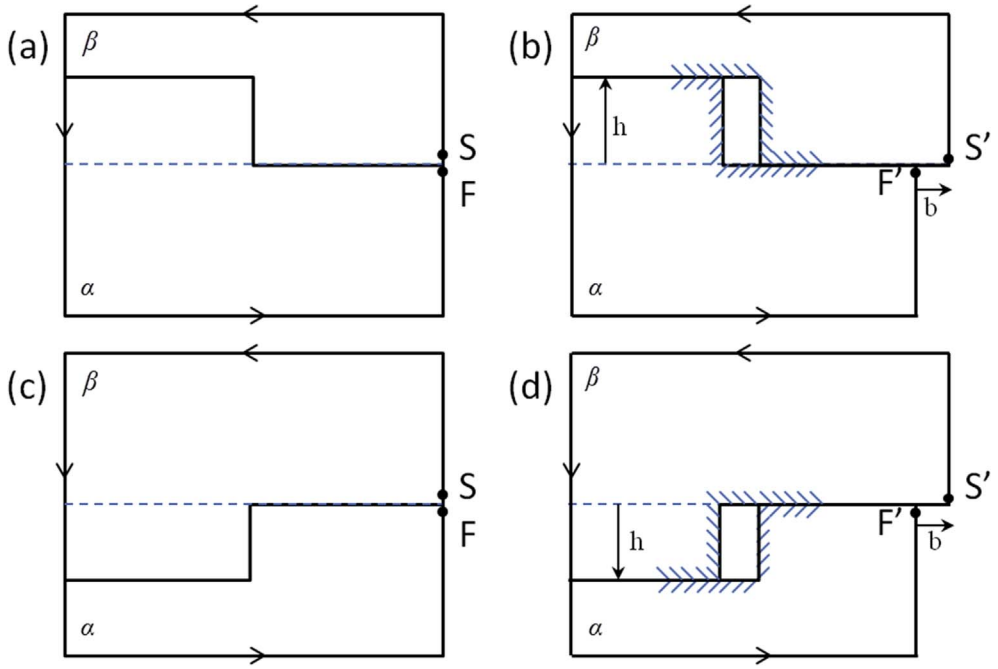

Fig. 10. Disconnection model for the <100> ledge, strained configuration (a), relaxed configuration (b), and the <110> ledge, strained configuration (c), relaxed configuration (d). The points (F′, S′) of the relaxed configuration are images of the points (F, S) of the current configuration in the inverse elastic distortion. The vector **F′S′** is the true Burgers vector **b** conventionally obtained from the oriented Burgers circuit starting at points (S, S') and finishing at points (F, F'). (b, h) are the Burgers vector and step magnitudes. The corresponding surfaces of crystals α and β are complementary, but the disconnections are not pure steps because their different positions in the reference configuration destroy this complementarity.

boundary value problems. As a natural consequence, the motion of the dislocation and step components of ledges is governed by dynamic laws of a similar nature, consistent with the observation of ledges propagating as persistent objects along grain boundaries (Rajabzadeh et al., 2013). Interestingly, dislocation and g-disclination fields built on the example of the present analysis may serve as

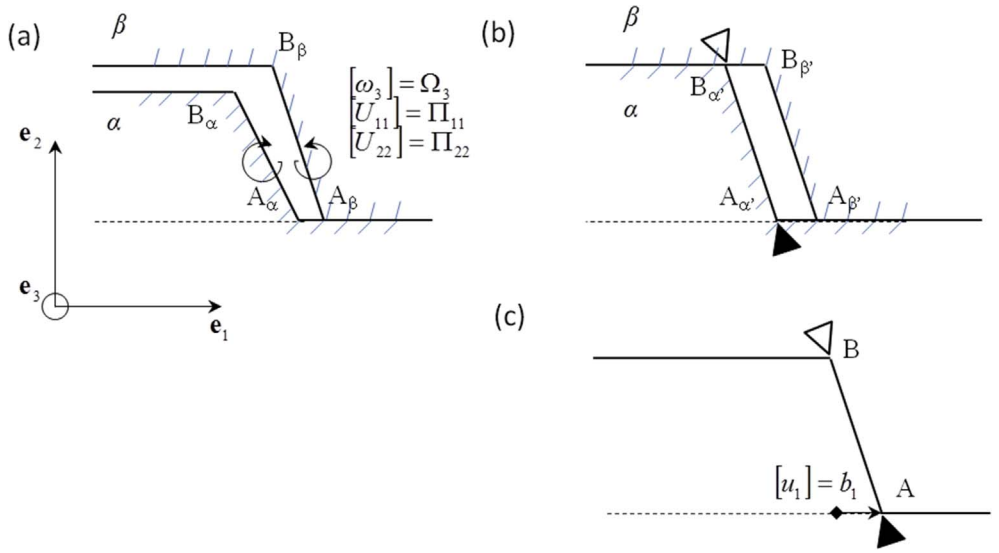

Fig. 11. Sketch of ledge model using dislocations and g-disclinations. Relaxed configuration (a), step configuration obtained in the presence of the g-disclination dipole (b), strained configuration (c). Bonding the corresponding surfaces $A_\alpha B_\alpha$ and $A_\beta B_\beta$ of crystals (α, β) into AB requires: (i) the rotation and stretch discontinuities of $A_\alpha B_\alpha$ with respect to $A_\beta B_\beta$: $[\![\omega_3]\!] = \Omega_3$, $[\![U_{11}]\!] = \Pi_{11}$, $[\![U_{22}]\!] = \Pi_{22}$ to render the crystals surfaces complementary from (a) to (b) (presence of g-disclinations and incompatibility of second-order distortion) and, (ii) the displacement discontinuity $[\![u_1]\!] = b_1$ to effectively bond the crystals surfaces in a translation of one crystal with respect to the other from (b) to (c) (presence of dislocations and incompatibility of first-order distortion). A standard disclination of Frank vector $[\![\omega_3]\!] = \Omega_3$ and a dislocation of Burgers vector $[\![u_1]\!] = b_1$ would be sufficient to match the surfaces $A_\alpha B_\alpha$ and $A_\beta B_\beta$ if they had same length: $[\![U_{11}]\!] = [\![U_{22}]\!] = 0$. The filled and open triangles indicate the g-disclination dipole.

initial conditions in the determination of the eventual dynamics of crystal defect ensembles. Examples of such solutions for the evolution of displacement, dislocation and disclination fields in straight tilt boundaries were provided in (Taupin et al., 2013, 2014; Cordier et al., 2014). Hence, the present analysis opens avenues for the study of the elastic properties of imperfect boundaries featuring ledges, their interactions with extrinsic crystal defects such as impiging dislocations or triple junctions, and for the prediction of their spatio-temporal evolutions, particularly in relation with their migration under stress. Comparisons with experimental measurements on grain boundary migration could then allow for a proper identification of the involved ledge mobility laws.

Acknowledgements

This work was supported by funding from the European Research Council under the ERC Grant No. 290424 RheoMan.

Appendix A. Supplementary data

Supplementary data related to this article can be found at http://dx.doi.org/10.1016/j.ijplas.2018.02.003.

Appendix A. Mathematical notations

A bold symbol denotes a tensor. When there may be ambiguity, an arrow is superposed to represent a vector: $\vec{\mathbf{V}}$. The transpose of tensor$\mathbf{A}$ is denoted by $\mathbf{A}^t$. The tensor $\mathbf{A}\cdot\mathbf{B}$, with rectangular Cartesian components $A_{ik}B_{kj}$, results from the dot product of tensors $\mathbf{A}$ and $\mathbf{B}$, and $\mathbf{A}\otimes\mathbf{B}$ is their tensorial product, with components $A_{ij}B_{kl}$. The vector $\mathbf{A}\cdot\mathbf{V}$, with rectangular Cartesian components $A_{ij}V_j$, results from the dot product of tensor $\mathbf{A}$ and vector $\mathbf{V}$. A: represents the trace inner product of the two second-order tensors $\mathbf{A}$: $\mathbf{B} = A_{ij}B_{ij}$, in rectangular Cartesian components, or the product of a higher order tensor with a second order tensor, e.g., $\mathbf{A}$: $\mathbf{B} = A_{ijkl}B_{kl}$. In the component representation, the spatial derivative with respect to a Cartesian coordinate is indicated by a comma followed by the component index. The cross product of a second-order tensor $\mathbf{A}$ and a vector $\mathbf{V}$ and the **curl** operation for second-order tensors are defined row by row, in analogy with the vectorial case. For any base vector $\mathbf{e}_i$ of the reference frame:

$$(\mathbf{A}\times\mathbf{V})^t\cdot\mathbf{e}_i = (\mathbf{A}^t\cdot\mathbf{e}_i)\times\mathbf{V} \tag{A.1}$$

$$(\mathbf{curl}\ \mathbf{A})^t\cdot\mathbf{e}_i = \mathbf{curl}(\mathbf{A}^t\cdot\mathbf{e}_i). \tag{A.2}$$

In rectangular Cartesian components:

$$(\mathbf{A}\times\mathbf{V})_{ij} = e_{jkl}A_{ik}V_l \tag{A.3}$$

$$(\mathbf{curl}\ \mathbf{A})_{ij} = e_{jkl}A_{il,k}, \tag{A.4}$$

where e_{jkl} is a component of the third-order alternating Levi-Civita tensor $\mathbf{X}$: $e_{jkl} = 1$ for even permutations of (j, k, l), $e_{jkl} = -1$ for odd permutations and $e_{jkl} = 0$ otherwise. For a third-order tensor $\mathbf{A}$, the components are:

$$(\mathbf{A} \times \mathbf{V})_{ijk} = e_{klm} A_{ijl} V_m \tag{A.5}$$

$$(\mathbf{curl}\ \mathbf{A})_{ijk} = e_{klm} A_{ijm,l}. \tag{A.6}$$

Note that (A.4, A.6) read

$$\mathbf{curl}\ \mathbf{A} = -\mathbf{grad}\ \mathbf{A} : \mathbf{X} \tag{A.7}$$

in intrinsic form.

References

Aaronson, H.I., 1962. In: Zackay, V.F., Aaronson, H.I. (Eds.), Decomposition of Austenite by Diffusional Processes. Interscience, New York, NY, pp. 387–546.
Acharya, A., Fressengeas, C., 2012. Coupled phase transformations and plasticity as a field theory of deformation incompatibility. Int. J. Fract. 174, 87–94.
Acharya, A., Fressengeas, C., 2015. Continuum mechanics of the interactions between phase boundaries and dislocations in solids. In: In: Chen, G.Q., Grinfeld, M., Knops, R.J. (Eds.), Differential Geometry and Continuum Mechanics, vol. 137. Springer Proceedings in Mathematics and Statistics, pp. 125–168.
Berbenni, S., Paliwal, B., Cherkaoui, M., 2013. A micromechanics-based model for shear-coupled grain boundary migration in bicrystals. Int. J. Plast. 44, 68–94.
Bilby, B.A., 1955. Types of dislocation source. In: Bristol Conference Report on Defects in Crystalline Solids. vol. 124 The Physical Society, London.
Cahn, J.W., Mishin, Y., Suzuki, A., 2006. Coupling grain boundary motion to shear deformation. Acta Mater. 54, 4953–4975.
Combe, N., Mompiou, F., Legros, M., 2016. Disconnections kinks and competing modes in shear-coupled grain boundary migration. Phys. Rev. B 93, 024109.
Combe, N., Mompiou, F., Legros, M., 2017. Shear-coupled grain-boundary migration dependence on normal strain/stress. Phys. Rev. Mat 1, 033605.
Cordier, P., Demouchy, S., Beausir, B., Taupin, V., Barou, F., Fressengeas, C., 2014. Disclinations provide the missing mechanism for deforming olivine-rich rocks in the mantle. Nature 507, 51–56.
Couillard, M., Radke, G., Botton, G.A., 2013. Strain fields around dislocation arrays in a Σ9 silicon bicrystal measured by scanning transmission electron microscopy. Philos. Mag. A 93, 1250–1267.
deWit, R., 1970. Linear theory of static disclinations. In: In: Simmons, J.A., deWit, R., Bullough, R. (Eds.), Fundamental Aspects of Dislocation Theory, vol. I. pp. 651–680 Nat. Bur. Stand. (US), Spec. Publ. 317.
Farkas, D., Froseth, A., Van Swygenhoven, H., 2006. Grain boundary migration during room temperature deformation of nanocrystalline Ni. Scripta Mater. 55, 695–698.
Frank, F.C., 1950. The resultant content of dislocations in an arbitrary intercrystalline boundary. In: Symposium on the Plastic Deformation of Crystalline Solids, Mellon Institute, Pittsburgh, (NAVEXOS-P-834), vol. 150.
Fressengeas, C., Taupin, V., Capolungo, L., 2014. Continuous modeling of the structure of symmetric tilt boundaries. Int. J. Solid Struct. 51, 1434–1441.
Fressengeas, C., Taupin, V., 2014. A field theory of distortion incompatibility for coupled fracture and plasticity. J. Mech. Phys. Solid. 68, 45–65.
Fressengeas, C., Taupin, V., 2016. A field theory of strain/curvature incompatibility for coupled fracture and plasticity. Int. J. Solid Struct. 82, 16–38.
Gertsman, Y.Yu, Nazarov, A.A., Romanov, A.E., Valiev, R.Z., Vladimirov, V.I., 1989. Disclination-structural unit model of grain boundaries. Philos. Mag. A 59, 1113–1118.
Gullett, P.M., Horstemeyer, M.F., Baskes, M.I., Fang, H., 2008. A deformation gradient tensor and strain tensors for atomistic simulations. Model. Simulat. Mater. Sci. Eng. 16, 015001.
Hirth, J.P., 1994. Dislocations, steps and disconnections at interfaces. J. Phys. Chem. Solid. 55, 985–989.
Hirth, J.P., Pond, R.C., 1996. Steps, dislocations and disconnections as interface defects relating to structure and phase transformations. Acta Mater. 44 4749–4163.
Li, J.C.M., 1972. Disclination model of high angle grain boundaries. Surf. Sci. 31, 12–26.
McDowell, D.L., 2010. A perspective on trends in multiscale plasticity. Int. J. Plast. 26, 1280–1309.
MacKain, O., Cottura, M., Rodney, D., Clouet, E., 2017. Atomic-scale modeling of twinning disconnections in zirconium. Phys. Rev. B 95, 134102.
Mishin, Y., Farkas, D., Mehl, M.J., Papaconstantopoulos, D.A., 1999. Interatomic potentials for monoatomic metals from experimental data and ab initio calculations. Phys. Rev. B 59, 3393–3407.
Plimpton, S.J., 1995. Fast parallel algorithms for short-range molecular dynamics. J. Comput. Phys. 117, 1–19.
Prieto-Depedro, M., Martin-Bragado, I., Segurado, J., 2015. An atomistically informed kinetic Monte Carlo model of grain boundary motion coupled to shear deformation. Int. J. Plast. 68, 98–110.
Rajabzadeh, A., Legros, M., Combe, N., Mompiou, F., Molodov, D.A., 2013. Evidence of grain boundary dislocation step motion associated to shear-coupled grain boundary migration. Philos. Mag. A 93, 1299–1316.
Rajabzadeh, A., Mompiou, F., Legros, M., Combe, N., 2014. Elementary mechanisms of shear-coupled grain boundary migration. Phys. Rev. Lett. 110, 265507.
Shih, K.K., Li, J.C.M., 1975. Energy of grain boundaries between cusp misorientations. Surf. Sci. 50, 109–124.
Spearot, D.E., Jacob, K.I., McDowell, D.L., 2007. Dislocation nucleation from bicrystal interfaces with dissociated structure. Int. J. Plast. 23, 143–160.
Sun, X.Y., Taupin, V., Fressengeas, C., Cordier, P., 2016a. Continuous description of the atomic structure of a grain boundary using dislocations and generalized-disclination density fields. Int. J. Plast. 77, 75–89.
Sun, X.Y., Cordier, P., Taupin, V., Fressengeas, C., Jahn, S., 2016b. Continuous description of a grain boundary in forsterite from atomic scale simulations: the role of disclinations. Philos. Mag. A 96, 1757–1772.
Sun, X.Y., Cordier, P., Taupin, V., Fressengeas, C., Karki, B.B., 2017. Continuous description of grain boundaries using crystal defect fields: the example of a 310/[001] tilt boundary in MgO. Eur. J. Mineral 29, 155–165.
Sutton, A.P., Vitek, V., 1983. On the structure of tilt grain boundaries in cubic metals. I. Symmetrical tilt boundaries. Phil. Trans. Roy. Soc. Lond. A 309, 1–68.
Taupin, V., Capolungo, L., Fressengeas, C., Das, A., Upadhyay, M., 2013. Grain boundary modeling using an elasto-plastic theory of dislocation and disclination fields. J. Mech. Phys. Solid. 61, 370–384.
Taupin, V., Capolungo, L., Fressengeas, C., 2014. Disclination mediated plasticity in shear-coupled boundary migration. Int. J. Plast. 53, 179–192.
Tucker, G.J., Zimmerman, J.A., McDowell, D.L., 2010. Shear deformation kinematics of bicrystalline grain boundaries in atomistic simulations. Model. Simulat. Mater. Sci. Eng. 18, 015002.
Tucker, G.J., Zimmerman, J.A., McDowell, D.L., 2011. Continuum metrics for deformation and microrotation from atomistic simulations: application to grain boundaries. Int. J. Eng. Sci. 49, 1424–1434.
Upadhyay, M.V., Capolungo, L., Taupin, V., Fressengeas, C., Lebensohn, R.A., 2016. A higher order elasto-viscoplastic model using fast Fourier transforms: effects of lattice curvatures on mechanical response of nanocrystalline metals. Int. J. Plast. 83, 126–152.
Volterra, V., 1907. Sur l'équilibre des corps élastiques multiplement connexes. Ann. Sci. Ecol. Norm. Sup. III 24, 401–517.
Wang, J., Beyerlein, I.J., Tomé, C.N., 2014. Reactions of lattice dislocations with grain boundaries in Mg: implications on the micro scale from atomic-scale calculations. Int. J. Plast. 56, 156–172.
Warner, D.H., Sansoz, F., Molinari, J.F., 2006. Atomistic based continuum investigation of plastic deformation in nanocrystalline copper. Int. J. Plast. 22, 754–774.
Zimmerman, J.A., Bammann, D.J., Gao, H., 2009. Deformation gradients for continuum mechanical analysis of atomistic simulations. Int. J. Solid Struct. 46, 238–253.